Heat-Flow Simulation of Laser Remelting with Experimental Validation

A.F.A. HOADLEY, M. RAPPAZ, and M. ZIMMERMANN

A transient three-dimensional (3-D) conduction-based heat-flow model has been developed in order to simulate the experimental processing conditions during laser surface remelting. This study concentrates on the validation of the model by comparison with data obtained from laser remelting experiments made in the eutectic alloy Al-Cu 33 wt pct over a range of traverse speeds between 0.2 and 5.0 m/s. It is shown that the simulation not only requires thermophysical data, but also a good knowledge of the laser beam process parameters. When the steady state is reached, the fusion isotherm which outlines the liquid pool yields the trace cross section and the resulting microstructure. Good agreement with experimental data is found over the range of processing speeds for the maximum melt pool dimensions, the transverse profile of the laser trace, the melt surface shape, and the resolidified microstructural spacings.

I. INTRODUCTION

LASER remelting is of commercial interest because of its ability to alter with accuracy the properties of very localized surface regions without reprocessing the material as a whole. However, it is this scale of operation which makes *in situ* measurements of the process variables so difficult. Most information is obtained by studying aftereffects, such as the change to the microstructure and the mechanical or chemical properties of the treated surface. Therefore, modeling the physical process can yield much insight into the complex phenomena occurring within the region activated by the moving high-power laser beam. Furthermore, modeling work can reduce substantially the time required for process optimization, scaleup, and control.

However, process modeling cannot be made in isolation from experimental work. The processing parameters which control the energy input to the workpiece influence directly the extent of the remelted region and thus must be determined with accuracy if the simulation is to give quantitative results. In particular, a special technique has been developed[1] for measuring the absorption, thus removing a considerable degree of uncertainty. The thrust of this paper is therefore in the systematic verification of a numerical model developed for the laser remelting process.

Although a number of conduction-based heat-transfer models for laser surface treatment, such as welding and remelting, have previously been published,[2-5] only a few[4,5] compare the simulation results directly with experiments. Those in Reference 4 consider only the width of the track for a single processing condition and this was overpredicted by 50 pct. Using the steady-state model which was the forerunner of the transient model presented here, Rappaz et al.[5] also calculated results which considerably overpredicted the melt widths, although the depths and the microstructure were accurately simulated.

Since these publications, many of the authors have now considered the effects of Marangoni convection and the free surface shape, thus further extending their simulation capabilities.[6-10] Again, only References 6, 9, and 10 make a direct comparison with the experimentally observed trace. Kou and Wang[6] achieved good agreement but for a single traverse speed of the laser beam of 4.2 mm/s which is at least two orders of magnitude lower than those speeds considered in this work. Furthermore, their measurement of the absorption by a calorimetric technique yielded an average value which did not distinguish between liquid and solid phases. Finally, the energy distribution was not known and a Gaussian distribution was assumed. Also, at low speeds, Paul and DebRoy[9] compared the melt pool shape, surface profile, and microstructure. The agreement with the experimental remelted profile was not particularly good, probably due to their two-dimensional (2-D) simulation. On the other hand, the predicted dendrite arm spacing was close to that observed. Finally, Zacharia et al.[10] considered the heat transfer during pulsed laser welding. Their 2-D simulation also gave good agreement for the microstructure with only qualitative agreement for the melt pool shape.

Besides the interest in aluminum-based alloys for industrial applications, Al-Cu 33 wt pct was chosen for this study for several other reasons.

(a) Being an alloy rather than a pure material, it is possible to distinguish clearly the remelted trace from the unmelted substrate.
(b) The thermophysical data are well defined.
(c) The eutectic microstructure for this alloy has been studied extensively, including high solidification rates.[11]
(d) The high conductivity of aluminum alloys reduces the effects of fluid flow in the melt pool which are not considered in the present simulation program.

In relation to the last point, melt pool convection is not particularly important at the high traverse speeds studied here, as the short interaction times and high forced advection lead to low levels of superheat. This can be observed from the Peclet number ($v_b\, a/\alpha$) based on the beam velocity, v_b, and radius, a, which varies in this study from 0.6 to 15. These high values apply over the

A.F.A. HOADLEY, Scientific Collaborator, M. RAPPAZ, Group Leader, and M. ZIMMERMANN, Graduate Student, are with Ecole Polytechnique Fédérale de Lausanne, Départment des Matériaux, Laboratoire de Métallurgie Physique, MX-G Ecublens, 1015 Lausanne, Switzerland.

whole pool depth, whereas with Marangoni convection, the strongest flow is confined to a region of the melt close to the surface.

The numerical model presented in this study is a transient three-dimensional (3-D) finite difference program. The transient algorithm was developed by extending an existing steady-state program[5] in order to simulate strongly coupled nonlinear conditions, thus allowing actual experimental conditions to be accurately portrayed. The results of the simulation are compared directly with the experiments over the widest range of processing conditions possible. Emphasis is placed on the agreement in the melt pool shape as observed from the surface and also from sections through the remelted trace.

II. THE HEAT-FLOW MODEL

A. *The Physical Model*

Average or enthalpy methods offer a versatile approach to modeling phase change problems. By assuming that phase equilibrium applies throughout, conditions within the processed material are given directly by the temperature or enthalpy of the material, thus avoiding any necessity to locate phase boundaries. The relationship between temperature, T, and enthalpy, H, is given by

$$H(T) = \int_0^T c(T') \, dT' + (1 - f_s(T))L \qquad [1]$$

where $c(T)$ and L are the volumetric specific heat and latent heat, respectively. The solid fraction f_s is deduced from a Scheil or Brody-Flemings model in the case of dendritic solidification or may be a step function if solidification is planar, as occurs with pure or eutectic material.

Figure 1 shows schematically the region modeled. It considers only the heat-affected zone around the laser beam, implicitly assuming that the workpiece is significantly larger than this volume. In an Eulerian coordinate system, the equation of energy of the material moving with velocity, $-v_b$, relative to the laser beam is given by

$$\frac{\partial H}{\partial t} - v_b \frac{\partial H}{\partial \xi} = \text{div} \, (\kappa(T) \, \text{grad} \, (T)) \qquad [2]$$

where κ is the temperature-dependent conductivity and ξ is the traverse direction (shown parallel to the x-axis). Note that any convection due to fluid flow in the molten region is not considered here.

Equations [1] and [2] are solved within the region Ω with the internal boundaries Γ_1 (Figure 1) chosen so that the temperature at the edge of the calculation domain is close to the initial temperature T_a of the base material. More precisely, the boundary condition at Γ_1 is specified by the Rosenthal point source model:[12]

$$T(\xi, r) = T_a + \frac{\bar{\beta}P}{2\pi\bar{\kappa}r} \exp\left\{\frac{-v_b(\xi + r)}{2\bar{\alpha}}\right\} \; (\xi, r) \in \Gamma_1$$

$$[3]$$

where r is the radial distance from the point heat source, P is the power of the heat source, and $\bar{\alpha}$, $\bar{\beta}$, and $\bar{\kappa}$ are
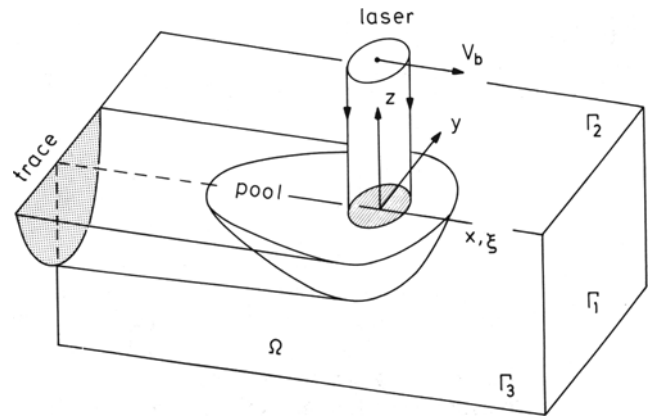

Fig. 1 — Schematic of the heat-affected region showing the shape of the melt pool and the resulting trace during continuous laser remelting.

the average thermal diffusivity, surface absorption, and thermal conductivity, respectively.

The surface of the material Γ_2 is assumed to remain flat during laser remelting, thus neglecting the effects of surface tension and gas pressure on the liquid region. The laser energy is distributed (Figure 1) depending on the configuration of the specific laser and the optical characteristics of its focusing mirrors. To simulate accurately the conditions in the immediate vicinity of the beam, the model utilizes a normalized one-dimensional radial function $F(\rho)^*$ given by a polynomial or sum-

---

*A normalized radial function means that $2\pi \int_0^\infty F(\rho) \cdot \rho \, d\rho = 1$.

---

mation of Gaussian functions which best fit the particular laser energy distribution. This function is then numerically integrated in order to find the local energy, q_i, impinging on each mesh:

$$q_i = P \int_{\Delta X_i} d\xi \int_{\Delta Y_i} dy \cdot F(\rho[\xi, y]) \qquad [4]$$

where ΔX_i and ΔY_i are the length and width (*i.e.*, along the ξ- and y-axes), respectively, of the mesh.

Since there is also heat loss to the surroundings by natural convection and radiation, the boundary condition on the surface Γ_2 is given by

$$\kappa \frac{\partial T}{\partial z} = \beta(T)PF(\rho) - h(T) \, (T(\xi, y) - T_a) \, (\xi, y) \in \Gamma_2$$

$$[5]$$

where $h(T)$ is a temperature-dependent heat-transfer coefficient and $\beta(T)$ is the temperature-dependent surface absorption. As only half of the laser trace is modeled, an adiabatic boundary condition is set on the longitudinal plane of symmetry Γ_3. The initial temperature field is simply the ambient temperature T_a.

B. *Numerical Formulation*

A finite difference method is used to solve Eq. [2] in three dimensions. Taking the fully implicit backward difference time discretization and performing volume integrations around each node in the mesh (see

Appendix A for details) leads to the following system of equations which can be represented in matrix form as

$$\left[\frac{M}{\Delta t} - V\right]\mathbf{H}^{n+1} + K^{n+1}\mathbf{T}^{n+1} = \mathbf{f}^{n+1} + \frac{M}{\Delta t}\mathbf{H}^n \quad [6]$$

where n is the time-step level. Implicit in Eq. [6] is an upwind procedure for the advection of enthalpy[13] which minimizes any oscillations occurring due to the imposed boundary at the downstream face.

A Newton method is employed to linearize the temperature as a function of the enthalpy in Eq. [1]. On substitution, Eq. [6] is then solved linearly for enthalpy by an optimized successive over-relaxation scheme. The convergence for each time-step is based on the maximum change in temperature between successive iterations, and when only one corrective iteration is required, the time-step length for the next step is increased, thereby accelerating the rate at which the steady state is approached. The steady-state temperature field is said to have been reached when the total change in energy within the mesh is less than 0.1 pct of the energy absorbed.

Finally, it is worth making one comment about the stability of the scheme. When average methods are employed, discontinuities are known to cause problems due to the spatial discretization. However, the use of a time-stepping scheme as applied here can prevent oscillation from occurring. For example, with an absorption in the liquid phase almost twice that of the solid phase, the program still converges smoothly, because the melt pool can only grow with time. The previous steady-state solution[5] did not converge under these conditions.

III. EXPERIMENTAL

The experiments were performed using a 1.5 kW CO_2 continuous wave laser. The processing conditions (Table I) were of a medium-to-high traverse speed and a focused beam, i.e., with a power intensity of 2.3×10^{10} W/m^2. While the beam characteristics were kept constant for each experiment, the traverse speed was varied through more than one order of magnitude. The minimum (0.2 m/s) was set by the onset of plasma formation which, at lower speeds, was observed to increase the energy transfer to the surface of the material to an extent where keyholing occurred and material was lost by vaporization. Around the maximum speed, 3.0 to 5.0 m/s, remelting was no longer complete: the trace was not continuous and showed regions where no fusion had occurred.

Experiments were conducted with two different experimental configurations. In the majority of tests, the laser energy impinged perpendicularly to the specimen

Table I. Laser-Processing Conditions

Laser power	1250 W
Focal diameter	260 μm
Beam mode	TEM00 + TEM10*
Traverse velocity	0.2 to 5.0 m/s
Ambient temperature	20 °C
Surface heat-transfer coefficient	100 W/m^2/°C
Protective gas	He

surface. However, a small number of experiments were conducted with the surface of the specimen slightly inclined relative to the laser beam. The first configuration allows part of the reflected energy to reenter the laser resonator, thus slightly increasing the laser power output. In the second orientation, this is not possible.

The focal diameter, power, and beam structure were measured using the following techniques. The total power impinging on the workpiece was determined using two similar commercially available calorimeters. The beam mode was obtained from PLEXIGLAS* burn prints pro-

---

*PLEXIGLAS is a trademark of Rohm & Haas Company, Philadelphia, PA.

---

duced by subjecting PLEXIGLAS blocks to laser pulses which cause vaporization of the polymer in proportion to the local power delivered. The positive of such a print is shown in Figure 2(a) and corresponds to a near top hat TEM00 + TEM10* mode. The remelting experiments were conducted at maximum energy intensity, and thus the size of the beam at the focal point was also determined. This was achieved using a rapid scan of the laser beam on a PLEXIGLAS plate inclined at an angle of 5 deg with the beam axis. The focal diameter was determined by measuring the width of the vaporized track at its narrowest point (Figure 2(b)). The value obtained was 260 ± 5μ.

The experimental results were analyzed by using micrographs of the specimen surface and of transverse sections. The transverse sections were obtained by cutting the specimen perpendicular to the laser trace. They were then polished down to a 1-μm diamond finish and etched using a Keller solution. The top surface was viewed without any metallographical preparation.

IV. RESULTS

A. Experimental Results

Figure 3(a) shows the transverse section of the trace with the remelted region clearly distinguishable from the base material. The maximum half width and depth of the remelted trace are measured directly from these micrographs to an accuracy of the order of 1 μm, but due to melt pool fluctuations, the pool shape can vary along the length of the trace and therefore it is necessary to make several micrographs. In the case of the configuration with the surface normal to the beam, experiments at each speed were repeated several times and the results for both the trace half widths and depths were found to have a standard deviation of approximately 7 μ.

Figure 3(b) is a photograph of the remelted surface obtained with a traverse speed of 0.2 m/s. The ripples produced by the nonsteady movement of the free melt surface outline the extent of the solidifying portion of the melt pool. The surface roughness after laser treatment was measured and was not found to exceed 6 μm peak-to-peak, which represents less than 5 pct of the total depth. The surface was even smoother at higher processing speeds, thus the assumption that the surface was flat appears to be justified. Also seen in the photograph (Figure 3(b)) is some evidence of oxidation at the edge of the melt pool.
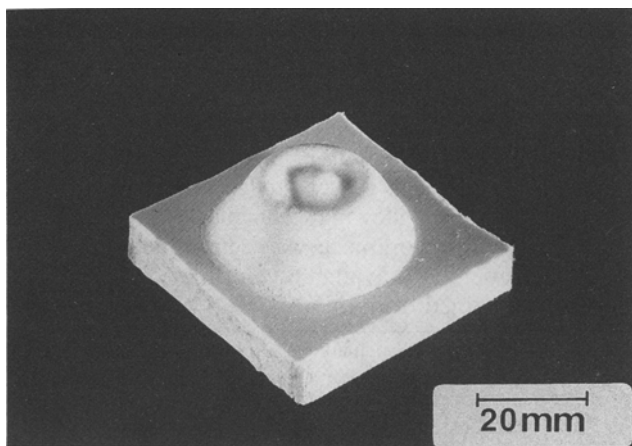
(a)
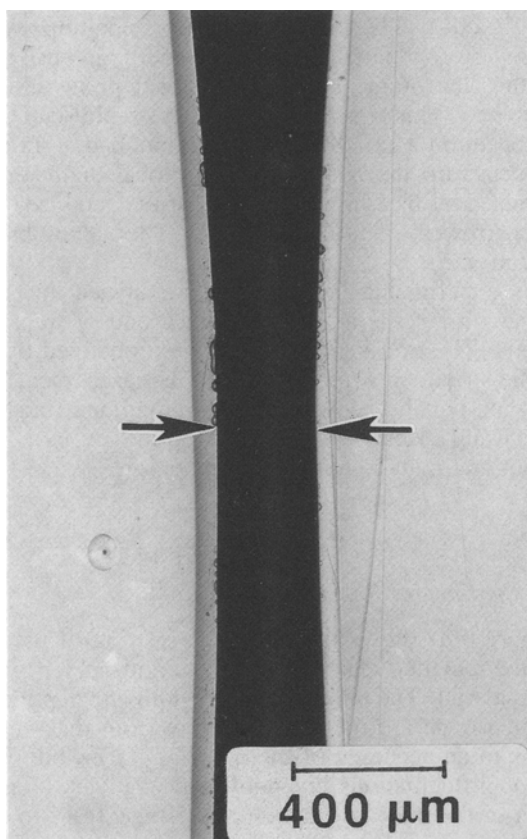
(b)

Fig. 2—Experimental determination of the energy distribution: (a) positive in silicon rubber of a burn print in PLEXIGLAS, made in front of the focalizing mirror (1250 W, 10 s); (b) imprint at the focal point, obtained by making a rapid scan (1250 W, 0.5 m/s) on a PLEXIGLAS plate inclined at 5 deg to the beam.

B. Simulation Results

Figure 4 shows a 3-D view of the calculated steady-state temperature field for a traverse velocity of 1.0 m/s. Also depicted is the finite difference enmeshment showing the mesh refinement in the region of the melt pool and the cross section of the simulated energy distribution, i.e., the function $F(\rho)$. For the simulation, the function $F(\rho)$ was best fitted using three identical Gaussian
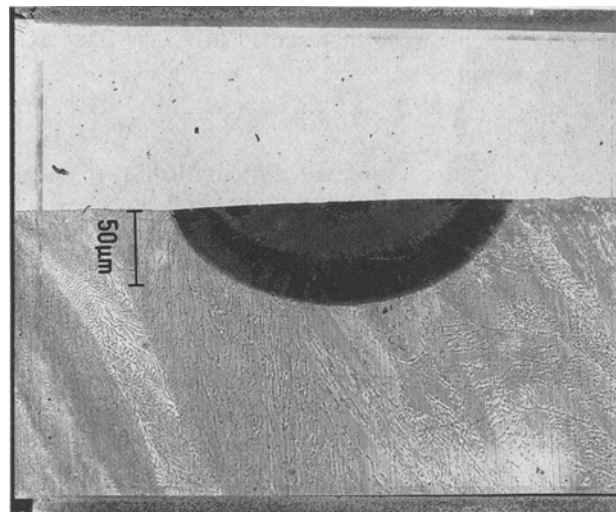
(a)
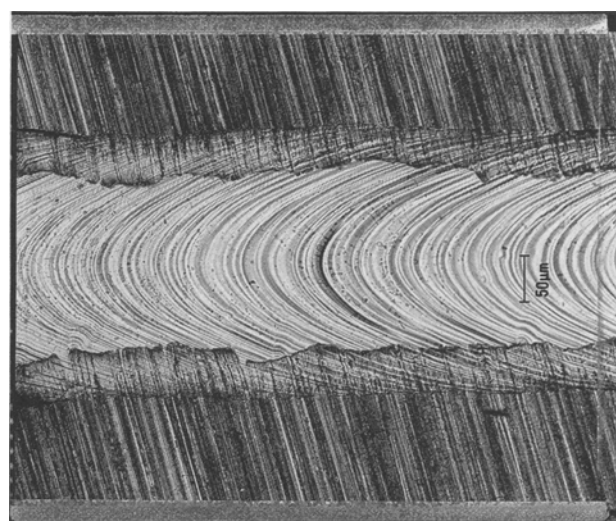
(b)

Fig. 3—Experimental analysis of the remelted trace: (a) micrograph of the transverse section of a trace made at 1.0 m/s and (b) photograph of the melt pool surface of a trace made at 0.2 m/s.

distributions. One distribution was centered on the axis $x = 0$ and the other two were offset an equal distance to either side. The superimposition of the three curves was rotated about the axis $x = 0$ to yield a circular distribution. Therefore, in order to match exactly the energy distribution observed experimentally in Figure 2(a), two parameters were adjusted: the standard deviation of the Gaussian functions and the offset between the centers of each curve. These two parameters are combined in such a way as to correspond with the measured beam radius (Figure 2(b)). It was found that the minimum energy to vaporize the PLEXIGLAS was two standard deviations from the center of the outer curves. Thus, for the specific laser configuration of these remelting experiments, the measured beam radius, a, was best reproduced by using an offset from the origin of $7/13a$ and a standard deviation of $2\sigma = 6/13a$. This yielded the form of the energy distribution observed in Figure 4 which may be compared with Figure 2.
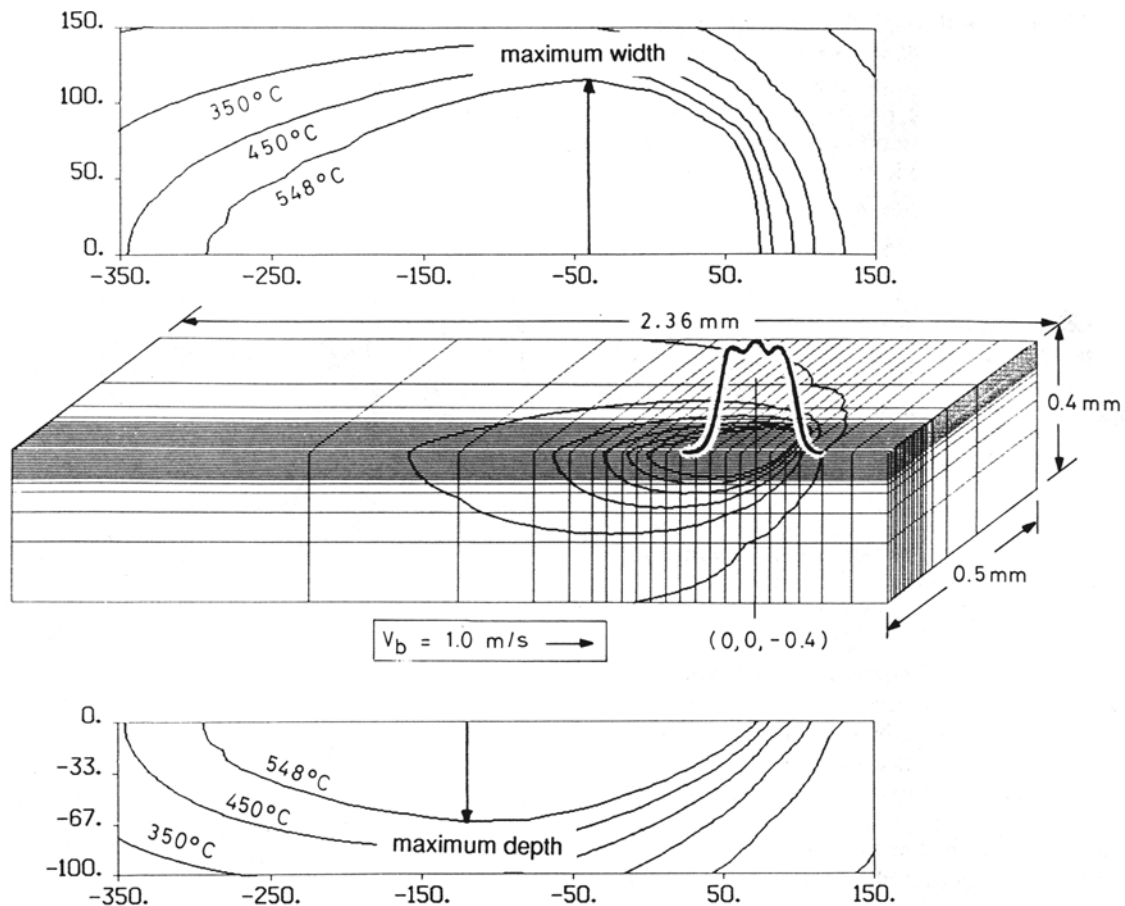
Fig. 4—3-D view of the calculated temperature field for 1.0 m/s traverse velocity showing also the computational mesh and a cross section of the laser beam energy distribution. The enlarged views of the surface and the longitudinal planes show the melt pool maximum dimensions.

In the calculation, the convective heat-transfer coefficient between the surface and the surrounding atmosphere was estimated to be 100 W/m^2/°C (Table I). The accuracy of this value was not particularly important, since the heat loss from the surface was always at least one order of magnitude smaller than the heat conducted out of the internal boundaries of the region being modeled.

Table II gives the thermophysical data for the Al-Cu 33 wt pct eutectic alloy which were necessary for the simulation. Important here is the value of the absorption in the solid and, particularly, the liquid phases. The absorption of Al-Cu 33 wt pct was measured using a calorimetric technique during laser remelting under the same conditions.[1] The values obtained were in good agreement with those of pure aluminum measured by an ellipsometric technique under high vacuum.[16]

Figure 4 also shows an enlarged view of the temperature profile for the surface and the central longitudinal plane. The point of maximum width, y^{max}, can be determined by taking the maximum perpendicular distance from the surface centerline to the first eutectic isotherm. In the same way, the maximum depth, z^{max}, is obtained by taking the maximum vertical distance in the longitudinal plane. Note, however, that the location of the point of maximum depth is always behind (ξ direction) the point of maximum width due to the time required for the heat to be transported from the surface to the bottom of the pool. Because of this, a transverse slice of the

Table II. Thermophysical Data Al-Cu 33 Wt Pct Eutectic

Eutectic composition	32.7 wt pct Cu	Ref. 11
Eutectic temperature	548.0 °C	Ref. 11
Surface absorption (solid)	$3.0 + 2.5 \times 10^{-3} T$ pct	Ref. 1
Surface absorption (liquid)	8.5 pct	Ref. 1
Density	3600 Kg/m^3	*
Specific heat (solid)	$2.6 \times 10^6 + 1.22 \times 10^3 T$ J/m^3/°C	**
Specific heat (liquid)	2.86×10^6 J/m^3/°C	**
Latent heat	1.23×10^9 J/m^3	Ref. 14
Thermal conductivity (solid)	125 W/m/°C	Ref. 15
Thermal diffusivity (average)	4.21×10^{-5} m^2/s	***

* = determined experimentally, ** = calculated from the constituent elements, and *** = calculated from the other properties.

melt pool in the yz plane through the point of maximum depth or width does not show the correct shape or extent of the remelted trace. Instead, the trace boundary is obtained by taking the point of maximum depth for each xz plane in the positive y direction or the point of maximum width for each xy plane in the negative z direction.

V. DISCUSSION

First considering the results over the whole range of processing speeds, it is convenient to use the nondimensionalization suggested by Kou et al.[2] Basing the characteristic length scale on the beam radius, a, the adimensional melt pool width and depth become

$$y^* = y^{max}/a \qquad [7]$$

$$z^* = z^{max}/a$$

The time scale is given by the ratio of the average diffusivity to advective transport:

$$t^* = \bar{a}/av_b \qquad [8]$$

Measuring and calculating the maximum half width and depth of traces made at several traverse velocities result in the dimensionless plots shown in Figure 5. On the same diagram, data points are shown for the two experimental configurations. For the orientation with the surface normal to the beam, vertical error bars indicate the experimental deviation. For the experiments with the specimen inclined, the measured data points are depicted with circles.

The maximum velocity and minimum processing time to achieve complete remelting are represented in Figures 5(a) and (b) by the point where the results cross the abscissa. As can be seen in this figure, melting was still possible at 5.0 m/s with the specimen normal to the beam, while with the inclined specimen, melting was observed only up to 3.0 m/s. However, the simulation results (squares) at the minimum processing time fall almost exactly between the two sets of experimental points.

Considering Figure 5(a), the maximum melt pool half widths, the agreement between simulation and experiment is excellent over the whole range of processing times above the minimum. The maximum depths depicted in Figure 5(b) also give good agreement for processing times up to the maximum, i.e., minimum velocity 0.2 m/s. However, the trend is for the melt depths to be overpredicted by the simulation as the processing time increases. The most likely explanation is that at long processing times, an outward flow generated by capillary forces maintains the surface of the melt at a relatively uniform temperature. By contrast, in the simulation, convection is not simulated and the peak temperature on the surface increases sharply with increasing time under the laser beam. Hence, the component of the diffusive flux acting downward from the surface would be increased by comparison with a convecting melt. This would account for the greater pool depths found in the simulation. Following the same reasoning, one would expect surface convection to produce greater melting near the surface. However, this is not reflected in Figure 5(a), as there is no apparent divergence between the experimental and the predicted maximum widths.
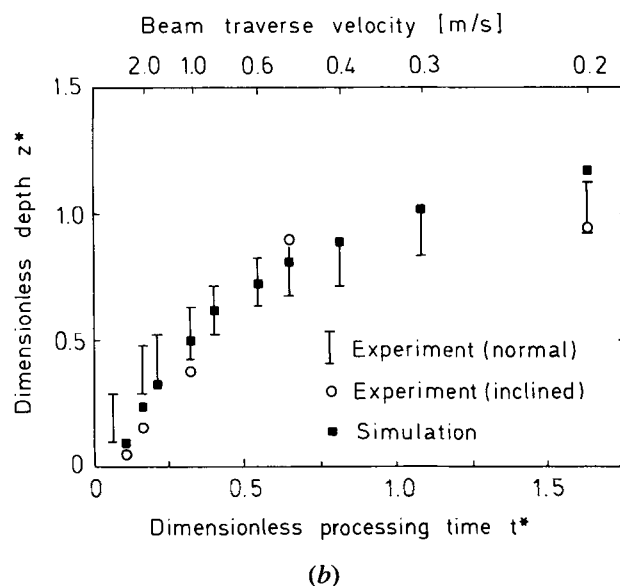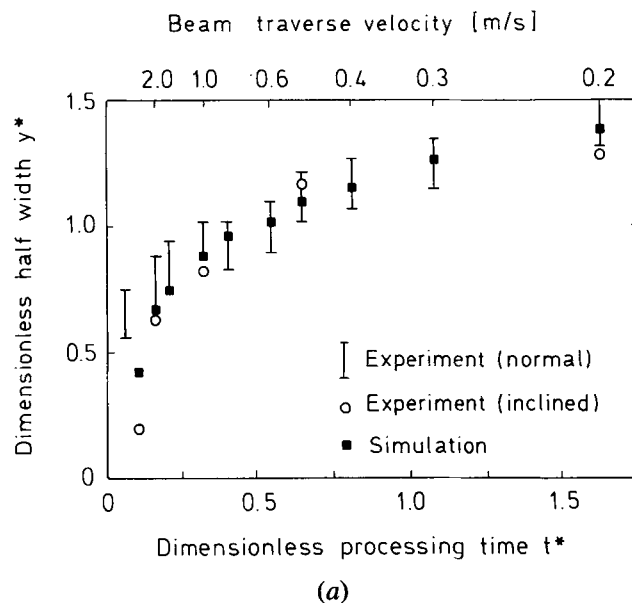

Fig. 5—Dimensionless plots of the melt pool dimensions with processing time: (a) maximum half width of the melt and (b) maximum depth of the melt.

Good simulation of the transverse section of the laser trace is important, as this outlines the exact region reprocessed for each pass of the laser. Such information is necessary when considering overlapping traces used to cover the whole of a surface region. The experimental transverse profiles were digitized from transverse micrographs, such as the one shown in Figure 3(a), and were then smoothed with a least-squares polynomial. These lines are shown in Figures 6(a) through (c) for traverse velocities of 0.5, 1.0, and 2.0 m/s, respectively, together with the points representing the interface position calculated from the numerical simulation. In all three cases, the overall shape is reproduced well by the simulation.

Figures 7(a) and (b) are the digitized curves (shown as the dashed lines) of typical surface ripples at 0.2 and 0.5 m/s taken from surface photographs, such as that shown in Figure 3(b). The base of the curve is taken
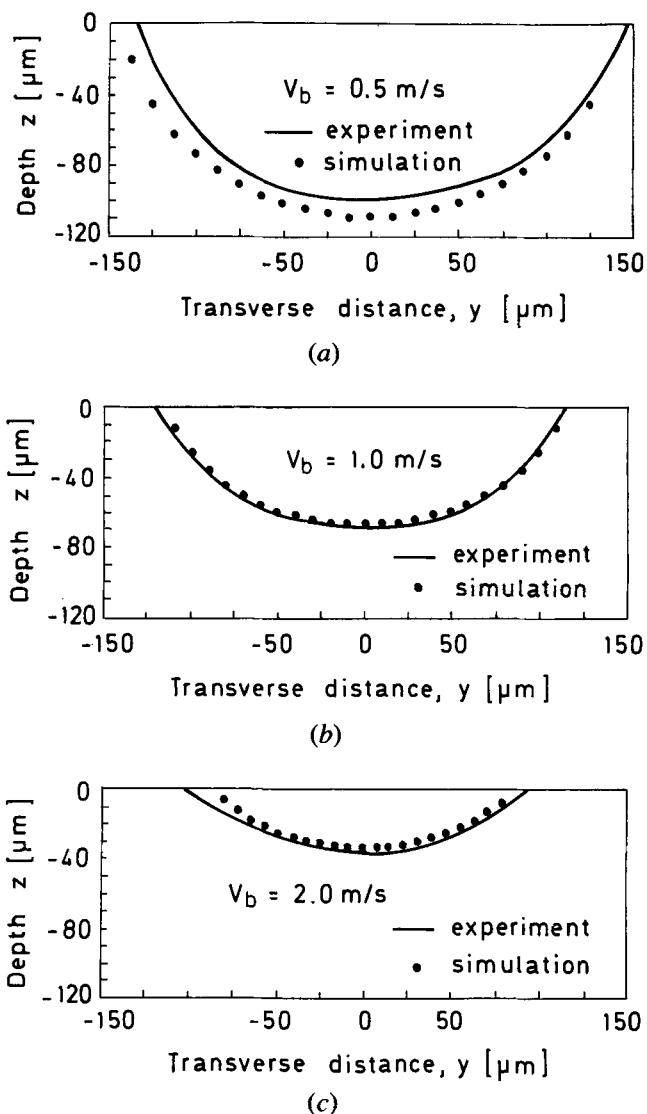
Fig. 6—Transverse sections of the remelted trace for traverse velocities: (a) 0.5 m/s, (b) 1.0 m/s, and (c) 2.0 m/s.

Fig. 7—Experimental and computed melt pool surface shapes for traverse velocities: (a) 0.2 m/s and (b) 0.5 m/s.

from the widest point corresponding to y^{max}, and the back of the pool is taken to be the turning point along the centerline of the trace. Unfortunately, the surface shapes at higher speeds could not be obtained, as the surface ripples were no longer regular or easily distinguishable above 0.5 m/s. For the simulated melt surface, it is also possible to show the shape of the region at the front of the pool undergoing fusion. The simulation curves shown as the continuous lines are superimposed in Figures 7(a) and (b) for comparison. In both cases, the predicted surface shape agrees well with the shape outlined by the ripples. However, at the lower speed, the experimental length of the pool is slightly shorter than predicted, while at the higher speed, it is significantly longer. The extension of the pool with increasing speed is most probably due to nonequilibrium conditions at the solidifying interface, evidenced experimentally by the formation of new metastable phases.[11] Since the solidification rate is the greatest on the centerline top surface, the interfacial undercooling will also be the largest at the tail of the pool. Using the eutectic growth model of Trivedi et al.,[17] the maximum undercooling was calculated for the two

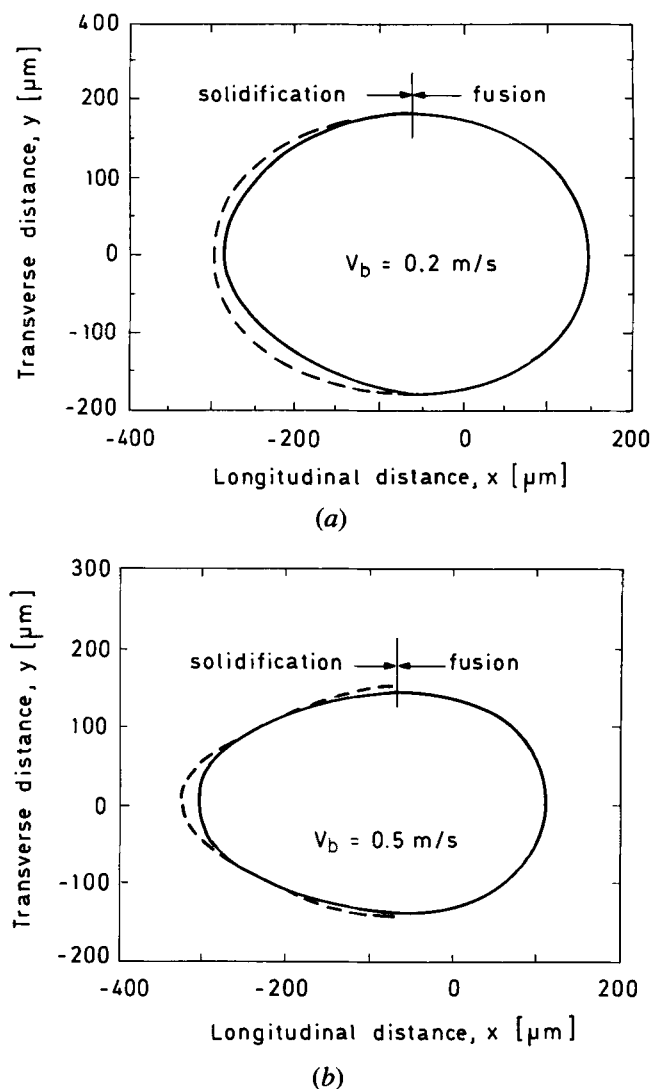traverse speeds indicated in Figure 7 to be of the order of 50 °C and 100 °C, respectively. By comparison with thermal equilibrium at the solid/liquid interface, this undercooling represents a significant reduction in the interface temperature and thus also a smaller temperature gradient available for heat removal through the solid.

With the pool shape determined, it is possible to simulate the microstructure formed in the remelted zone using the microscopic model of eutectic growth[17] and following the coupling procedure developed by Carrupt et al.[18] Due to the formation of metastable phases at higher speeds,[11] only the lowest processing velocity (0.2 m/s) was evaluated. The eutectic interlamellar spacings measured by transmission electron microscopy (TEM) and the predicted curve for the central longitudinal plane are shown in Figure 8. In this figure, the eutectic spacing is plotted as a function of the height from the bottom of the pool rather than the depth below the surface due to the discrepancy between the predicted and the measured pool depths. The agreement with the experimental data is excellent. However, the interlamellar spacing comparison in itself is not a good validation of the pool shape
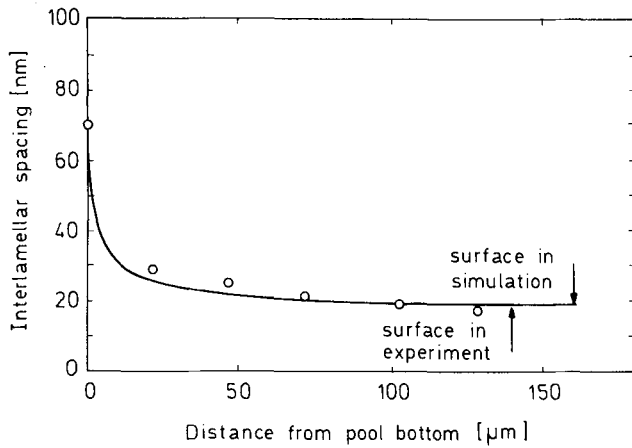
Fig. 8—Comparison between the measured and the calculated eutectic interlamellar spacings taken on the central longitudinal plane for a traverse velocity of 0.2 m/s. The circles depict the points measured by TEM.

because of the $v^{-1/2}$ dependence for eutectic growth.[17] Instead, the minimum value of spacing is more related to the parameters of the microscopic model. Hence, this explains why References 5 and 18 both obtained reasonable agreement for the microstructural spacing, having at the same time, large discrepancies in the melt pool dimensions. Nevertheless, the sharp decrease in spacing with height is well described by the simulation, proving its value as a tool for microscopic prediction within the macroscopic simulation.

VI. CONCLUSION

The aim of this study was to compare in detail the experimental and numerical results for the melt pool shape under the high-speed processing conditions of laser remelting. The agreement between the predicted results and the experimental data was very good, to within 10 pct over the whole range of processing speeds, except at the very highest speeds where the orientation of the piece relative to the laser beam was found to have a significant influence on the experiment. This reliability can be attributed mainly to modeling accurately the laser energy distribution as affected by the actual laser configuration and the absorption of the alloy. Hence, the importance of determining these variables experimentally is stressed if good qualitative results are desired. However, two features not simulated were identified as being important. At short processing times, high interfacial undercooling associated with very high solidification rates was shown to have an effect on the shape of the melt surface. This was seen by the extension of the length of the pool behind the beam. At the other extreme, long interaction times giving rise to stronger convective effects meant that the simulation overpredicted the pool depth. In order to widen the range of processing conditions and alloys that may be accurately simulated, it is necessary to encompass these two phenomena. Interfacial undercooling may require a different numerical approach, as non-equilibrium conditions encountered in columnar solidification are not handled easily by average methods.[19] In considering Marangoni convection, much effort should

be expended in obtaining experimental data in order to test the validity of the many implicit assumptions involved in numerical fluid mechanics.

APPENDIX A

A brief derivation of the finite difference form of the heat equation in three dimensions

The heat equation, Eq. [2], is solved using a finite difference scheme on an orthogonal mesh. Considering a grid point, C, within the volume, Ω, and its six neighbors (Figure A1), Eq. [2] can be integrated over the volume, $\Delta X \Delta Y \Delta Z$, of the mesh. Using the divergence theorem and integrating $(\partial H/\partial \xi) \cdot d\xi$, the following relationship is obtained:

$$\Delta X \Delta Y \Delta Z \frac{\partial H}{\partial t} = \int_{\Gamma_c} \kappa(T) \cdot \text{grad } T \cdot \mathbf{n} \cdot d\Gamma_c$$

$$+ v_b \cdot \int_{\Delta Y} dy \int_{\Delta Z} dz \cdot [H_R - H_L] \quad \text{[A1]}$$

where $\mathbf{n}$ is the unit vector normal to the surface, Γ_c and H_R and H_L represent the average enthalpy at the right and left of C, respectively. Introducing an upwind parameter, θ, the enthalpy difference in Eq. [A1] can be written as

$$v_b \cdot \int_{\Delta Y} dy \int_{\Delta Z} dz \cdot [H_R - H_L] = v_b \cdot \Delta Y \Delta Z$$

$$\cdot [H_E \theta + H_c(1 - 2\theta) + H_w(\theta - 1)]$$

$$\text{with } 1/2 \le \theta \le 1 \quad \text{[A2]}$$

Using Eq. [A2], Eq. [A1] becomes

$$\kappa_{EC} \frac{\Delta Y \Delta Z}{\Delta X_E} (T_E - T_C) + \kappa_{WC} \frac{\Delta Y \Delta Z}{\Delta X_W} (T_W - T_C)$$

$$+ \kappa_{NC} \frac{\Delta X \Delta Y}{\Delta Z_N} (T_N - T_C) + \kappa_{SC} \frac{\Delta X \Delta Y}{\Delta Z_S} (T_S - T_C)$$

$$+ \kappa_{FC} \frac{\Delta X \Delta Z}{\Delta Y_F} (T_F - T_C) + \kappa_{BC} \frac{\Delta X \Delta Z}{\Delta Y_B} (T_B - T_C)$$

$$+ v_b \cdot \Delta Z$$

$$\cdot [H_E \theta + H_C(1 - 2\theta) + H_W(\theta - 1)]$$

$$= \Delta X \Delta Y \Delta Z \frac{\partial H_C}{\partial t}$$

$$\text{[A3]}$$

The thermal conductivities appearing in Eq. [A3], κ_{ic} with $i = E, W, N, S, B, F$, correspond to $\kappa(T_{iC})$ taken at the midtemperature, $T_{iC} = (T_i + T_C)/2$. Following Thomasset,[13] a stable and accurate scheme can be obtained for the linear case, i.e., when $H(T) = cT$ with

$$\theta = \frac{1}{2}\left[1 + \coth\left(\frac{\gamma}{2}\right)\right] - \frac{1}{\gamma} \quad \text{with } \gamma = \frac{v_b \cdot \Delta X}{\kappa/c} \quad \text{[A4]}$$
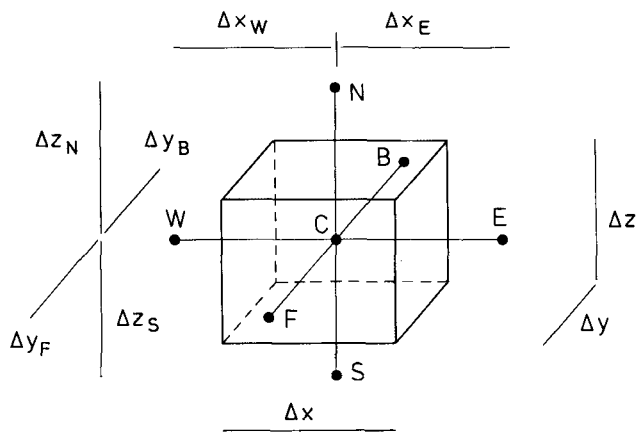
Fig. A1 — Schematic showing the 3-D configuration of nodes around an internal grid point.

Taking the backward difference approximation for the temporal derivative and accounting for the boundary conditions for the nodes of $\Gamma_1 \cup \Gamma_2 \cup \Gamma_3$, the matrix equation (Eq. [6]) is obtained:

$$\left[\frac{M}{\Delta t} - V\right]\mathbf{H}^{n+1} + K^{n+1}\mathbf{T}^{n+1} = \mathbf{f}^{n+1} + \frac{M}{\Delta t}\mathbf{H}^n \quad [A5]$$

where M = mass matrix;
K = conductivity matrix;
V = matrix of advection;
$\mathbf{f}$ = vector of boundary conditions;
$\mathbf{T}$ and $\mathbf{H}$ = vectors of nodal temperatures and enthalpies, respectively; and
n = time-step level.

ACKNOWLEDGMENTS

REFERENCES

1. A. Frenk, A.F.A. Hoadley, and J.-D. Wagnière: *Metall. Trans. B*, 1991, vol. 22B, pp. 138-40.
2. S. Kou, S.C. Hsu, and R. Mehrabian: *Metall. Trans. B*, 1981, vol. 12B, pp. 33-45.
3. T. Chande and J. Mazumder: *J. Appl. Phys.*, 1984, vol. 56, pp. 1981-86.
4. K.V. RamaRao and J.A. Sekhar: *Acta Metall.*, 1987, vol. 35, pp. 81-87.
5. M. Rappaz, B. Carrupt, M. Zimmermann, and W. Kurz: *Helvetica Phys. Acta*, 1987, vol. 60, pp. 924-36.
6. S. Kou and Y.H. Wang: *Metall. Trans. A*, 1986, vol. 17A, pp. 2265-70.
7. C.L. Chan, R. Zehr, J. Mazumder, and M.M. Chen: *Modeling and Control of Casting and Welding Processes*, TMS, Warrendale, PA, 1986, pp. 229-46.
8. T. Zacharia, A.H. Eraslan, and D.K. Aidun: *Modeling and Control of Casting and Welding Processes IV*, TMS, Warrendale, PA, 1988, pp. 177-85.
9. A. Paul and T. DebRoy: *Metall. Trans. B*, 1988, vol. 19B, pp. 851-58.
10. T. Zacharia, S.A. David, J.M. Vitek, and T. DebRoy: *Metall. Trans. A*, 1989, vol. 20A, pp. 957-67.
11. M. Zimmermann, M. Carrard, and W. Kurz: *Acta Metall.*, 1989, vol. 37, pp. 3305-13.
12. J.F. Lancaster: *Metallurgy of Welding*, George Allen & Unwin Pub., London, 1980, p. 42.
13. F. Thomasset: *Implementation of Finite Element Methods for Navier-Stokes Equations*, Springer-Verlag, New York, NY, 1981, pp. 37-40.
14. M.H. Burden and H. Jones: *J. Inst. Met.*, 1970, vol. 98, pp. 249-52.
15. M. Gündüz and J.D. Hunt: *Acta Metall.*, 1985, vol. 33, pp. 1651-72.
16. M. Brückner, J.H. Schaefer, and J. Uhlenbusch: *J. Appl. Phys.*, 1989, vol. 66, pp. 1326-32.
17. R. Trivedi, P. Magnin, and W. Kurz: *Acta Metall.*, 1987, vol. 35, pp. 971-80.
18. B. Carrupt, M. Rappaz, and M. Zimmermann: *Modeling and Control of Casting and Welding Processes IV*, TMS, Warrendale, PA, 1988, pp. 581-91.
19. M. Rappaz: *Int. Mater. Rev.*, 1989, vol. 34, pp. 93-123.